

# The importance of finite-temperature exchange-correlation for warm dense matter calculations

Valentin V. Karasiev,\* Lázaro Calderín, and S.B. Trickey  
*Quantum Theory Project, Dept. of Physics and Dept. of Chemistry,  
 University of Florida, Gainesville FL 32611-8435*

(Dated: 13 May 2016)

Effects of explicit temperature dependence in the exchange-correlation (XC) free-energy functional upon calculated properties of matter in the warm dense regime are investigated. The comparison is between the KSDT finite-temperature local density approximation (TLDA) XC functional [Phys. Rev. Lett. **112**, 076403 (2014)] parametrized from restricted path integral Monte Carlo data on the homogeneous electron gas (HEG) and the conventional Monte Carlo parametrization ground-state LDA XC functional (Perdew-Zunger, “PZ”) evaluated with  $T$ -dependent densities. Both Kohn-Sham (KS) and orbital-free density functional theory (OFDFT) are used, depending upon computational resource demands. Compared to the PZ functional, the KSDT functional generally lowers the direct-current (DC) electrical conductivity of low density Al, yielding improved agreement with experiment. The greatest lowering is about 15% for  $T = 15$  kK. Correspondingly, the KS band structure of low-density fcc Al from KSDT exhibits a clear increase in inter-band separation above the Fermi level compared to the PZ bands. In some density-temperature regimes, the Deuterium equations of state obtained from the two XC functionals exhibit pressure differences as large as 4% and a 6% range of differences. However, the Hydrogen principal Hugoniot is insensitive to explicit XC  $T$ -dependence because of cancellation between the energy and pressure-volume work difference terms in the Rankine-Hugoniot equation. Finally, the temperature at which the HEG becomes unstable is  $T \geq 7200$  K for  $T$ -dependent XC, a result that the ground-state XC underestimates by about 1000 K.

PACS numbers: 51.30.+i, 05.30.-d, 71.15.Mb, 52.25.Fi

## I. INTRODUCTION

Warm dense matter (WDM), characterized by elevated temperatures and wide compression ranges, plays an important role in planetary-interior physics and materials under extreme conditions, including the path to inertial confinement fusion, heavy ion beam experiments, and Z-pinch compression experiments [1–6]. Development of computational and theoretical methods to treat WDM applications is important both for interpreting experimental results and for gaining insight about thermodynamic regions that are difficult to access experimentally.

Current practice is to treat the WDM electronic degrees of freedom via finite-temperature density functional theory (DFT) [7–9]. That necessitates use of an approximate exchange-correlation (XC) free-energy density functional,  $\mathcal{F}_{xc}[n(T), T]$ . A common approximation [10–12] is to use a ground-state XC functional evaluated with the finite- $T$  density, that is  $\mathcal{F}_{xc}[n(T), T] \approx E_{xc}[n(T)]$ . This is the “ground state approximation” or GSA. Ref. 13 presented a rationale for why the GSA might be expected to work well. The essence of that argument is that GSA automatically fulfills certain constraints. The present study gives clear demonstrations of GSA deficiencies for specific systems in certain thermodynamic conditions and physical properties. The study involves systematic investigations of three essential questions. What properties are

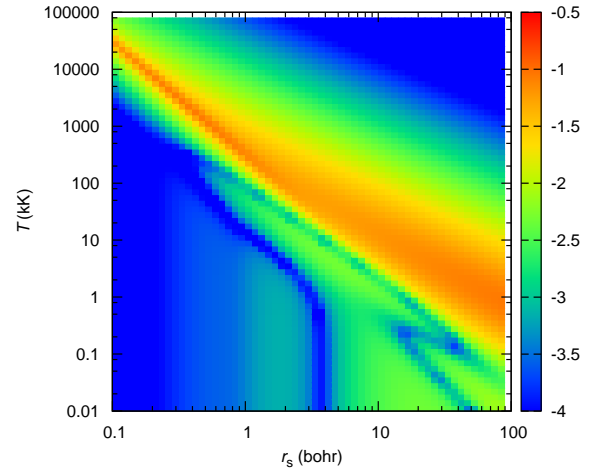


FIG. 1: Map in  $(r_s, T)$  plane which shows the relative importance of explicit  $T$ -dependence in the exchange-correlation free-energy functional for the HEG measured as  $\log_{10}(|f_{xc}(r_s, T) - e_{xc}(r_s)| / (|f_s(r_s, T)| + |e_{xc}(r_s)|))$ .

affected by the explicit  $T$ -dependence of  $\mathcal{F}_{xc}$ , over what thermodynamic regime does the dependence manifest itself, and what are the magnitudes of the effects?

For compactness in what follows we use the phrase “XC thermal effects” as a shortened expression for “effects of the explicit  $T$ -dependence in the XC free energy”.

\*Electronic address: vkarasev@qtp.ufl.edu

Thus, XC thermal effects are those not included in the GSA. As orientation to the issue, Fig. 1 shows the relative importance of XC thermal effects as a function of  $r_s$  (the Wigner-Seitz radius,  $r_s = (3/4\pi n)^{1/3}$ ) and  $T$  as  $\log_{10}(|f_{xc}(r_s, T) - e_{xc}(r_s)| / (|f_s(r_s, T)| + |e_{xc}(r_s)|))$  for the homogeneous electron gas (HEG).  $f_{xc}$  is the XC free-energy per particle [14],  $e_{xc}$  is the zero- $T$  XC energy per particle [15], and  $f_s$  is the non-interacting free-energy per particle [16]. Note that this ratio is the difference of energies per particle for two small quantities divided by the energy per particle for what, in most cases, is a larger quantity. In particular, the denominator of the ratio always is greater than or equal to the magnitude of the free energy per particle (calculated with the zero- $T$  exchange-correlation):  $|f_s| + |e_{xc}| \geq |f_s + e_{xc}|$ . The ratio therefore generally underestimates the significance of XC thermal effects.

The orange and yellow regions of Fig. 1 indicate the  $(r_s, T)$  domain wherein one may expect the  $T$ -dependence of XC to be important for accurate predictions. The nearly diagonal orange-yellow band is particularly useful for insight. First, it shows that finite- $T$  XC may be expected to be important at low  $T$  for large  $r_s$  values. Second, that  $T$ -dependence in XC dwindles in importance in the large- $T$  limit. Thus the relative importance ratio has a maximum at some intermediate temperature which depends on  $r_s$ . In terms of the reduced temperature,  $t = T/T_F$  ( $T_F = (1/2)(9\pi/4)^{2/3}r_s^{-2}$  the Fermi temperature), the near diagonal orange-yellow band in Fig. 1 is rendered in the  $(r_s, t)$  plane as a roughly horizontal band with a lower border starting at  $t \approx 0.3$  for  $r_s = 0.1$  and rising to  $t \approx 1$  for  $r_s = 100$ . That band is narrowest at low  $r_s$  and broadens by over a factor of 100 at  $r_s = 100$ .

This plain analysis of a fundamentally important many-fermion system motivates investigation of XC thermal effects upon the calculated properties of real inhomogeneous systems. There have been a few previous studies, [17–22] but all except one used  $T$ -dependent XC functionals [23–26] constructed from various approximations to the underlying many-fermion theory, not from parametrization to path-integral Monte Carlo (PIMC) data. They also involved other approximations, e.g., ensemble averaging of core-hole pseudopotentials in Ref. 17, average-atom and related schemes [18, 19], and Car-Parrinello MD in Ref. 20. For equations of state (EOS), Hugoniot shock compression curves, and conductivities, Refs. 17–19 predicted significant XC temperature effects, while Ref. 20 found only small differences for the electrical resistivity of Aluminum. Danel *et al.* [22] find consistent lowering of pressures from thermal XC effects and small effects on the Deuterium Hugoniot. The common limitation of all those studies was the uncontrolled nature of the local-density approximation (LDA) XC functionals they used. Ref. 21 did use the modern Karasiev-Sjostrom-Dufty-Trickey (KSDT) finite-temperature local density approximation (TLDA) [14] for  $\mathcal{F}_{xc}$  but showed results only for the equation of

state of Deuterium at relatively high material density (small- $r_s$ ) and concluded that the fractional pressure shifts relative to ground-state LDA were small, though not of one sign.

In contrast, the present work provides an assessment of XC thermal effects on the basis of KSDT [14] for several properties in diverse systems and state conditions. KSDT was parametrized solely to quantum Monte Carlo (QMC) plus restricted path integral Monte Carlo (RPIMC) simulation data for the HEG [27, 28] and rigorous limiting behaviors. KSDT therefore is the consistent counterpart to the widely used Perdew-Zunger (PZ) [15] LDA functional, which is a parametrization of ground-state HEG QMC data. Lack of consistency between the PZ parametrization and some earlier finite- $T$  LSDA approximations was noted explicitly as a problem in Ref. 20.

The next Section gives details about the KSDT finite- $T$  and PZ XC functionals along with the basics of the methodology employed, including monitoring of entropy positivity. Section III A presents Kubo-Greenwood conductivity calculations on Aluminum for those two functionals, as well as the KS band structures of fcc Aluminum at comparable densities and temperatures. Sections III B–III C provide the corresponding KSDT vs. PZ comparison for the Deuterium equation of state and for the liquid Hydrogen Hugoniot. Section III D gives a brief study of the equilibrium properties of the electron gas (both HEG and with a point charge compensating background) at finite- $T$ . Concluding discussion is in Sec. IV.

## II. METHODS

### A. Exchange-correlation free-energy functional

To reiterate, the KSDT finite- $T$  LDA XC free-energy functional [14] is a first-principles parametrization of RPIMC simulation data for the finite- $T$  HEG [27] and recent zero- $T$  QMC HEG data [28]. KSDT also has proper asymptotics and is free of unphysical roughness. Additionally, it fits the recent data from Schoof *et al.* [29] well. For the spin-unpolarized XC free-energy per particle, KSDT has the form

$$f_{xc}^u(r_s, t) = -\frac{1}{r_s} \frac{a(t) + b_u(t)r_s^{1/2} + c_u(t)r_s}{1 + d_u(t)r_s^{1/2} + e_u(t)r_s}. \quad (1)$$

The functions  $a(t)$  and  $b_u(t) - e_u(t)$  are tabulated in Ref. 14. Most calculations require evaluation of the XC free-energy,  $\mathcal{F}_{xc}[n, T] \equiv \int d\mathbf{r} n(\mathbf{r}) f_{xc}^u(r_s(\mathbf{r}), t(\mathbf{r}))$  and the corresponding functional derivative. Evaluation of properties which involve the internal energy (e.g. Hugoniot curves, heat capacities) requires the XC internal energy per particle as well. It follows via the standard thermodynamic relation  $\mathcal{S}_{xc} = -\partial\mathcal{F}_{xc}/\partial T|_{N, V}$  as

$$\varepsilon_{xc}^u(r_s, t) = f_{xc}^u(r_s, t) - t \left. \frac{\partial f_{xc}^u(r_s, t)}{\partial t} \right|_{r_s}, \quad (2)$$

so the corresponding XC internal energy is  $\mathcal{E}_{\text{xc}}[n, T] \equiv \int d\mathbf{r} n(\mathbf{r}) \varepsilon_{\text{xc}}^{\text{u}}(r_{\text{s}}(\mathbf{r}), t(\mathbf{r}))$ . Both Eqs. (1) and (2) are implemented in our PROFESS@QUANTUMESPRESSO interface [30–34]. (KSDT also has been implemented in LibXC [35] recently.) Also as noted above, the comparison ground-state XC functional evaluated with  $T$ -dependent densities is the well-known PZ LDA [15].

## B. Computational details

Both the KSDT and PZ functionals were used in *ab initio* molecular dynamics (AIMD) simulations. We used two forms of AIMD, with Kohn-Sham (KS) DFT forces and with orbital-free DFT (OFDFT) forces. For OFDFT, the non-interacting free energy functional  $\mathcal{F}_s$  we used was the recently developed VT84F approximation [36] in the case of the Deuterium equation of state and a semi-empirical “tunable” functional [37] for Al at low material density.

The KS calculations used standard projector-augmented-wave (PAW) pseudo-potential data sets [38] (three electrons in the valence for the Al atom), and PAWs transferable to high compressions [34, 39, 40], all generated with the ground state LDA XC. For calculations with PROFESS@Q-ESPRESSO, that LDA XC was PZ [15], while for those done with ABINIT (see below) it was the Perdew-Wang (PW) [41] XC. For the purposes of this study the difference in behavior between those two functionals is negligible [39]. The PAW data sets were generated at  $T = 0$  K. At the highest temperatures involved, thermal depopulation of the core levels treated by the PAWs is minuscule. To illustrate, the highest LDA KS Kohn-Sham eigenvalue among the frozen atomic Al core states is about -70 eV. At  $T = 30$  kK (the highest  $T$  of our Al calculations), the Fermi-Dirac occupation of that level depopulates by about  $10^{-12}$ . The underlying assumption (and common practice in WDM studies) therefore is that these PAW data sets are transferable to various thermodynamic conditions (i.e., the sets describe an effective core-valence interaction with valence electrons in various states). Therefore, one assumes validity for that core-valence interaction at finite- $T$  as well. Observe that use of the  $T$ -dependent KSDT XC functional in subsequent calculations does not introduce an inconsistency because the KSDT functional reduces de facto to the PZ functional in the zero- $T$  limit at which the PAW sets were generated.

Local pseudopotentials (LPPs) [34, 40, 42, 43] developed for OFDFT and also transferable to high compressions were used in the OFDFT calculations. For Hydrogen and Deuterium, the LPP only regularizes the bare Coulomb electron-nuclear interaction singularity, hence does not pose any possible transferability limitations for high- $T$  such as those for systems with core electrons, as just discussed.

The plane-wave energy cutoff was 500 eV for Al, and 1000 eV for Hydrogen and Deuterium. Further pertinent

details are in Sec. III B.

For conductivities, we did KS-AIMD simulations for  $T = 5, 10$  and in some cases for 15 kK with  $\Gamma$ -point-only sampling of the Brillouin zone, the PZ XC functional, and the PAW data set. At elevated temperatures,  $T = 15, 20,$  and 30 kK, and the low material densities of primary interest (see below), such KS-AIMD calculations proved to be unaffordable. In those circumstances, we used AIMD driven by OFDFT forces from a semi-empirical  $\mathcal{F}_s$  parametrized (“tuned”) to extrapolate KS pressure behavior into the low material density region. The reference for parametrization was KS pressure data for fcc Al at  $T = 8$  kK and material densities  $0.6 \leq \rho_{\text{Al}} \leq 2$  g/cm<sup>3</sup>. Procedural details will be published elsewhere [37]. The essential point here is that the AIMD generated a sequence of ionic configurations from which a sample set was selected (so-called “snapshotting”) for use in standard Kubo-Greenwood calculations [44, 45]. The OFDFT AIMD was performed using an LDA model LPP [42, 43], again with the PROFESS@Q-ESPRESSO interface [30, 31]. Depending on the particular material density, the AIMD was done with 16 or 32 atoms in the simulation cell such that the finite system size effects were small [11]. Conductivities were calculated as averages over two to ten well-separated AIMD snapshots using a  $2 \times 2 \times 2$  sampling of the Brillouin zone. The calculations used the PAW formalism and were done with a locally modified version of ABINIT [46–48] which included the KSDT XC free energy functional. We used a 3-electron PAW generated as prescribed in Ref. 38.

To gain insight and illustrate the origin of the XC-dependent differences in the Al DC conductivity results, a series of KS band structure calculations was done with the same PAW data set for fcc Al with density 0.2 g/cm<sup>3</sup> and  $T = 5, 10,$  and 20 kK. Those include 16, 28, and 80 bands respectively. Those calculations were highly converged for the fcc primitive unit cell with a  $12 \times 12 \times 12$  Monkhorst-Pack  $\mathbf{k}$ -grid [49].

The Hydrogen Hugoniot was studied with KS-AIMD forces up to  $T \leq 30$  kK, with 64 atoms in the simulation cell and a  $3 \times 3 \times 3$  Monkhorst-Pack  $\mathbf{k}$ -grid [49]. Because of computational demand issues, for  $T \geq 30$  kK, the KS-AIMD calculations used the Baldereschi mean value BZ point [50].

Finally, the various HEG stability and electron heat capacity calculations were performed with static background (or lattice) using KS and OFDFT respectively.

## C. Validation of approximate functionals for entropy positivity

Previously, we addressed [40] positivity of the entropy in OFDFT for a few generalized gradient approximation (GGA) non-interacting free-energy functionals  $\mathcal{F}_s^{\text{GGA}}$ . The entropy density in some cases was contaminated by local negative contributions. Such contamination typically leads to a small-magnitude contribution to the free

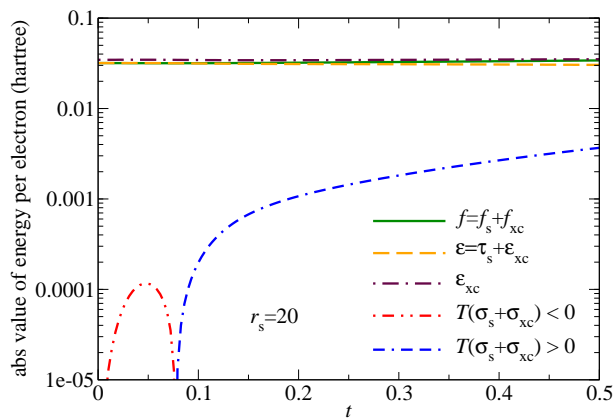


FIG. 2: The total free-energy, internal energy, internal XC energy and entropic component (per particle) magnitudes for the spin-unpolarized HEG for  $r_s = 20$  bohr calculated with the KSdT XC free-energy parametrization [14].

energy compared to the total  $T\mathcal{S}_s$  value. More critically, the global entropy value in all calculations was positive, consistent with the positivity constraint being on the entropy, not on the entropy density.

In the present work we monitored the sign of the total entropic contribution. For the orbital-free case, that consists of the non-interacting component

$$\mathcal{S}_s[n, T] = -\left. \frac{\partial \mathcal{F}_s[n, T]}{\partial T} \right|_{N, V}, \quad (3)$$

and the XC component (defined as a difference between the entropies of the interacting and non-interacting system  $\mathcal{S}_{xc} = \mathcal{S} - \mathcal{S}_s$ )

$$\begin{aligned} \mathcal{S}_{xc}[n, T] &= -\left. \frac{\partial \mathcal{F}_{xc}[n, T]}{\partial T} \right|_{N, V} \\ &= \frac{1}{T} \int d\mathbf{r} n(\mathbf{r}) (e_{xc}^u(r_s, t) - f_{xc}^u(r_s, t)). \end{aligned} \quad (4)$$

In our experience, the total entropy is *always* positive.

For the KSdT XC free-energy parametrization in Eq. (1), recently it was found [13] that the HEG total entropy becomes negative at very large  $r_s$  values and small temperatures (approximately  $r_s > 10$  and  $t < 0.1$ ). Practically that regime is irrelevant to real systems. Analysis of the corresponding entropic contribution to the free-energy confirms that. Fig. 2 shows that for  $r_s = 20$  bohr the negative entropic contribution has a maximum amplitude of order 0.0001 Hartree per electron. This error is negligible, since it is at or below the typical accuracy of finite-temperature Kohn-Sham and orbital-free codes. It is also negligibly small in comparison to the total free energy or total internal energy. The situation is quite similar for other large- $r_s$ . The violation is inconsequential, hence seems to be primarily of an aesthetic character.

After-the-fact validation of the thermal Kohn-Sham and orbital-free calculations in combination with the

KSdT XC free-energy parametrization Eq. (1) show that the total entropy is positive for all materials and all WDM conditions probed in the present work.

### III. RESULTS

#### A. Aluminum conductivity and band structure

Experimental study of the electrical conductivity of warm dense Al was reported in Ref. 51. Theoretical treatment via AIMD and the Kubo-Greenwood formula [44, 45] is found in Refs. 10, 11 and 20. That latter study found the influence of the finite- $T$  XC functional on the DC electrical resistivity (the inverse of electrical conductivity) to be small at material densities  $\rho_{Al} = 1.0$  and  $1.4$  g/cm<sup>3</sup> ( $r_s = 2.89$  and  $2.58$  bohr respectively, assuming the usual three free electrons) and  $T = 5 \rightarrow 20$  kK. The earlier studies [10, 11] found that DC conductivities depend weakly upon  $T$  in the range  $6 - 30$  kK for material densities between roughly  $0.5$  and  $2.0$  g/cm<sup>3</sup>. Since the total  $T$ -dependence in general is dominated by the non-interacting free-energy contribution and the XC contribution is comparatively small in magnitude (recall discussion of Fig. 1), those findings mean that for this density range XC thermal effects should be small as well.

However, the results of Refs. 10, 11 also suggest that XC thermal effects might be noticeable at low material densities (between  $0.025$  and  $0.3$  g/cm<sup>3</sup>). In that region, the DC conductivity has strong  $T$ -dependence. Figure 1 also suggests that XC thermal effects should be important at such low material densities (large- $r_s$ ) for temperatures between about  $10$  and  $500$  kK. (At  $T = 15$  kK the reduced temperature is  $t \approx 1.0$  and  $0.6$  for  $\rho_{Al} = 0.1$  and  $0.2$  g/cm<sup>3</sup> respectively.) These considerations motivated our AIMD calculations of the DC conductivities for three densities in that range,  $\rho_{Al} = 0.1, 0.2,$  and  $0.3$  g/cm<sup>3</sup> ( $r_s = 6.22, 4.94,$  and  $4.21$  bohr respectively). (Note that the foregoing  $r_s$  values are calculated with the conventional total number of valence electrons, 3, for Al. However, that could underestimate an effective free-electron  $r_s$  and thereby diminish the validity of correlation between XC thermal effects on a particular property (e.g., conductivity) and Fig. 1. Insight from that Figure depends to some extent on how  $r_s$  for a physical system is calculated.)

The average of the Kubo-Greenwood optical conductivity over a number of snapshots or configurations ( $N_{\text{config}}$ ) as a function of frequency  $\omega$  is given in atomic units by

$$\sigma(\omega) = \frac{1}{N_{\text{config}}} \sum_{I=1}^{N_{\text{config}}} \sum_{\mathbf{k}} w_{\mathbf{k}} \sigma_{\mathbf{k}}(\omega; \{\mathbf{R}\}_I), \quad (5)$$



with

$$\sigma_{\mathbf{k}}(\omega; \{\mathbf{R}\}_I) = \frac{2\pi}{3\omega\Omega} \sum_{i,j}^{N_b} \sum_{\nu=1}^3 (f_{i,\mathbf{k},I} - f_{j,\mathbf{k},I}) \times |\langle \varphi_{j,\mathbf{k},I} | \nabla_{\nu} | \varphi_{i,\mathbf{k},I} \rangle|^2 \delta(\epsilon_{j,\mathbf{k},I} - \epsilon_{i,\mathbf{k},I} - \omega) \quad (6)$$

Here  $\Omega$  is the system volume,  $w_{\mathbf{k}}$  is the weight of BZ point  $\mathbf{k}$ , and  $f_{i,\mathbf{k},I}$  are Fermi-Dirac occupations of KS orbitals  $\varphi_{i,\mathbf{k},I}$ . Those orbitals and associated eigenvalues  $\epsilon_{j,\mathbf{k},I}$  are indexed as band, BZ vector, and lattice configuration snapshot at lattice coordinates  $\{\mathbf{R}\}_I$ .

The DC conductivity is the limit of  $\sigma(\omega)$  as  $\omega \rightarrow 0$ . Because of the frequency-difference delta-function, computational convergence to that limit with respect to the number of KS bands ( $N_b$ ) is known to be rapid [11]. Consequences of the numerical implementation of the  $\delta$ -function are a complicating factor. Gaussian broadening of the  $\delta$ -function [10]  $\Delta = 0.2$  eV was used. Increasingly severe local oscillations in  $\sigma(\omega)$  appear rapidly as  $\Delta$  is decreased below that value, especially at lower temperatures. As a consequence, the DC conductivity does not converge as  $\Delta \rightarrow 0$ . See the discussion in Ref. [52]. The chosen value of  $\Delta$  is close to being optimal according to the criterion of Ref. [10] for the system size and density-temperature range relevant here. Admittedly, however, the results are sensitive to that choice. A better procedure would determine the optimal  $\Delta$  at each density and temperature.

To ensure convergence with  $N_b$ , our calculations used a minimum occupation number threshold of order  $10^{-6} - 10^{-7}$ , such that the number of bands included for  $\rho_{\text{Al}} = 0.1$  g/cm<sup>3</sup> was  $N_b = 208, 672, 1184, 1920,$  and  $3096$  at  $T=5, 10, 15, 20,$  and  $30$  kK respectively. The number of bands required decreases rapidly with increasing material density, but increases rapidly with increasing numbers of atoms in the simulation cell. The effect of these dependencies can be checked by testing for satisfaction of the  $f$ -sum rule[44]. It was satisfied to 90 – 92% at  $T = 5$  kK, and to 95 – 97% at higher temperatures.

Results are shown in Fig. 3. The standard deviations shown there as error bars correspond to averaging over the snapshots. Note first that for all  $T$ , the explicitly  $T$ -dependent XC functional lowers the DC conductivity. Beginning at  $T = 5$  kK, the effect increases with increasing  $T$  and is largest near  $T=15$  kK, then decreases. Fig. 4 shows the relative error in using the ground-state XC functional

$$\frac{|\Delta\sigma|}{\sigma^{\text{PZ}}} := \frac{|\sigma_{\text{DC}}^{\text{KSDT}} - \sigma_{\text{DC}}^{\text{PZ}}|}{\sigma_{\text{DC}}^{\text{PZ}}} \quad (7)$$

That error is 0.5%, 13%, 15%, 11%, and 7% for  $\rho_{\text{Al}} = 0.1$  g/cm<sup>3</sup> at  $T = 5, 10, 15, 20$  and  $30$  kK respectively. An important aspect is that the relative error is not amenable to correction by some simple, rule-of-thumb shift.

The number of snapshots at the lowest temperature,  $T = 5$  kK, is ten. Nevertheless the standard deviation at

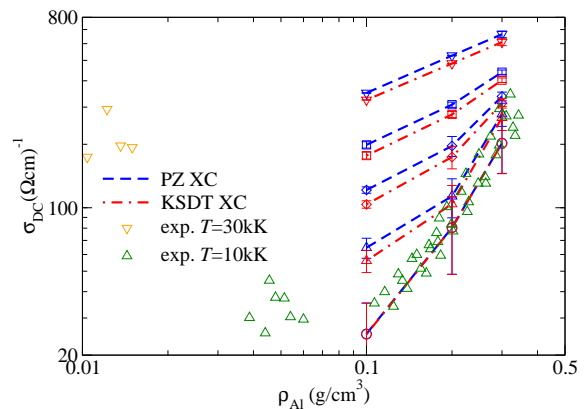


FIG. 3: Aluminum DC conductivity as a function of density from calculations with  $T$ -dependent KSDT (dot-dashed) and ground state PZ (dashed) XC functionals for five isotherms. From bottom to top  $T = 5$  kK (circles), 10 kK (triangles up), 15 kK (diamonds), 20 kK (squares) and 30 kK (triangles down). Experimental data [51] correspond to 10 kK (triangles up) and 30 kK (triangles down).

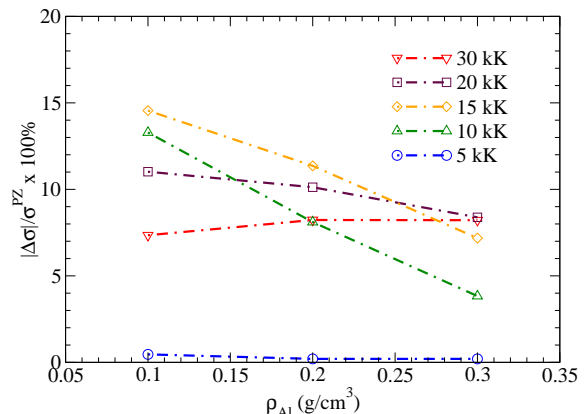


FIG. 4: Relative error in DC conductivity for Al as function of density for five different temperatures.

that  $T$  is large. To decrease it would require increasing the number of snapshots or the simulation cell size or both. Such sensitivity to the nuclear configuration may be explained by transient formation and dissociation of small Al clusters at that  $T$ , a process seen in the snapshots. Crucially, however, the difference between KSDT and PZ conductivities for each snapshot depends very weakly on nuclear configuration. Those differences, as shown in Figs. 3 and 4, are negligible at  $T = 5$  kK. As  $T$  increases, the standard deviation decreases as the system becomes more nearly uniform (10, 8 and 4 snapshots were used for  $T = 10, 15$  and  $20$  kK respectively) and the difference attributable to the two functionals becomes clearly discernible. Averaging over only two snapshots in fact provides very small error bars at the highest  $T = 30$  kK.

There exists also an implicit influence of  $T$ -dependent XC on DC conductivities via nuclear configurations.

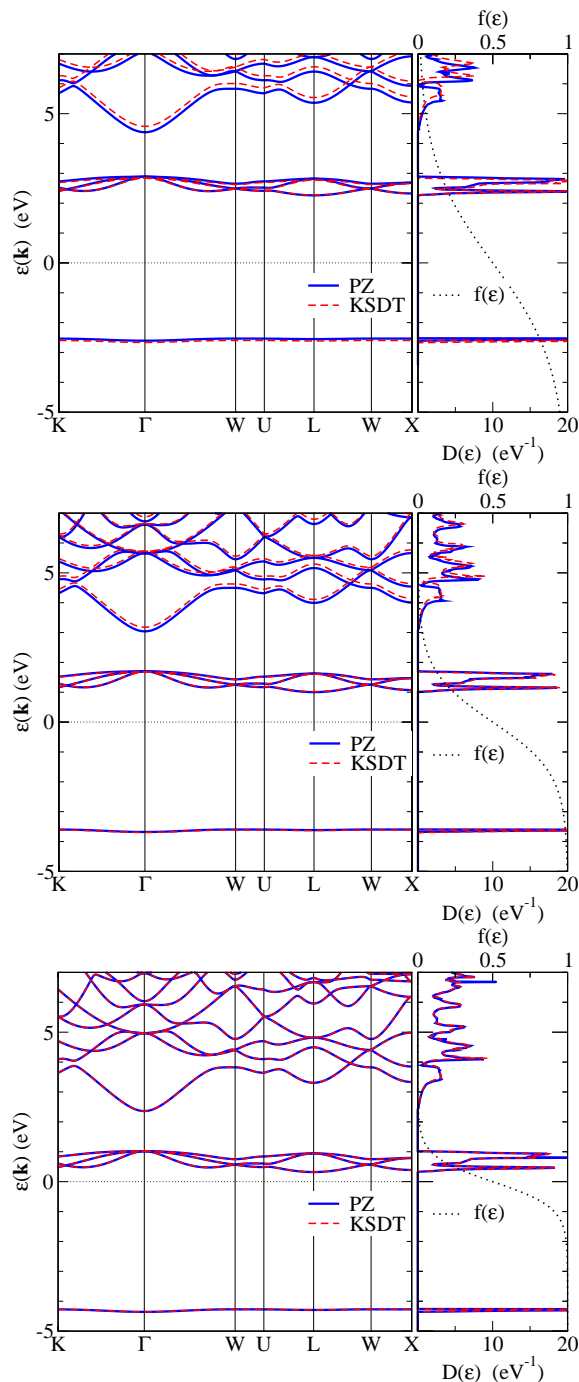


FIG. 5: Comparison of fcc Al KS band structures for  $\rho = 0.2\text{g/cm}^3$  from KSDT  $T$ -dependent XC and PZ ground-state XC for  $T = 5, 10, \text{ and } 20\text{kK}$  (bottom to top). Fermi level  $\epsilon_F$  set to zero. The right-hand panels display the density of states  $D(\epsilon)$  and Fermi-Dirac occupation  $f(\epsilon)$ .

That arises because a snapshot sequence from AIMD performed with the KSDT functional will differ from the sequence from the PZ functional (with  $T$ -dependent density of course). To identify only the *explicit* dependence, we deliberately used the same snapshots for both

KSDT and PZ conductivity calculations. Evaluation of the *implicit* influence would require calculations of averages over much longer snapshot sequences generated by AIMD with each XC functional. Given that it is almost certain that the implicit effects are small compared to the explicit ones, and given the cost of doing the AIMD calculations and snapshot conductivities (even with the cost effectiveness of OFDFT AIMD), we opted not to pursue the implicit influence.

Since the KS eigenvalues and orbitals are inputs to the Kubo-Greenwood calculations, direct examination of thermal XC effects upon the rather unfamiliar low-density KS band-structure therefore is of interest. Fig. 5 provides comparison of the fcc Al band structure at  $\rho = 0.2\text{ g/cm}^3$  at three temperatures. Overall there is a  $T$ -dependent shifting upwards of the bands above  $\epsilon_F$  as they become increasingly occupied. For energies nearest  $\epsilon_F$  on either side, the KSDT bands lie below the PZ ones, whereas that ordering is reversed for the bands next upward. In those bands, at  $T = 20\text{ kK}$  the shift is about  $0.2\text{ eV}$ , about  $10\%$  of the electronic temperature. That is also the amount of relative increase in inter-band separation between the band at the Fermi level and the next higher conduction band. The separation increase shows up as a lowering of  $\sigma(\omega)$  for small  $\omega$  induced by the lowering of Fermi-Dirac occupations and their derivatives (occupation number difference) in Eq. (6).  $D(\epsilon)$  clearly shows not only the general shift upward that accompanies increasing  $T$ , but also that the bandwidth nevertheless is essentially unchanged.

## B. Equation of state of warm dense Deuterium

To explore XC thermal effects upon bulk thermodynamics, we did KS and OFDFT AIMD calculations on Deuterium at material densities between  $0.2$  and  $10\text{ g/cm}^3$  for  $T = 2 \rightarrow 1000\text{ kK}$ . The familiar unfavorable computational cost scaling with  $T$  limited our KS-AIMD results to below  $T \approx 125 - 180\text{ kK}$  for higher material densities ( $\rho_D \geq 2\text{ g/cm}^3$ ), and up to  $T \approx 60 - 90\text{ kK}$  for  $\rho_D = 0.2$  and  $0.506\text{ g/cm}^3$ . Depending on the material density, the simulation cells had  $64, 128, \text{ or } 216$  atoms. For some KS-AIMD cases, the number of atoms in the simulation cell was decreased with increasing  $T$ . Most of the KS calculations were performed at the  $\Gamma$ -point only, though for  $\rho_D = 0.506\text{ g/cm}^3$  a  $2 \times 2 \times 2$  Monkhorst-Pack Brillouin zone grid [49] was used at the two lowest temperatures.

The pressure converges slowly with respect to the number of MD steps, but pressure differences (between simulations with two different XC functionals) typically converge more rapidly. At each density-temperature point, the system first was equilibrated for at least  $1500$  MD steps, followed by  $4500$  steps for data gathering. The first  $500$  of those steps were considered to be an additional equilibration, hence were discarded during calculation of statistic averages. For  $\rho_D = 0.506\text{ g/cm}^3$  at

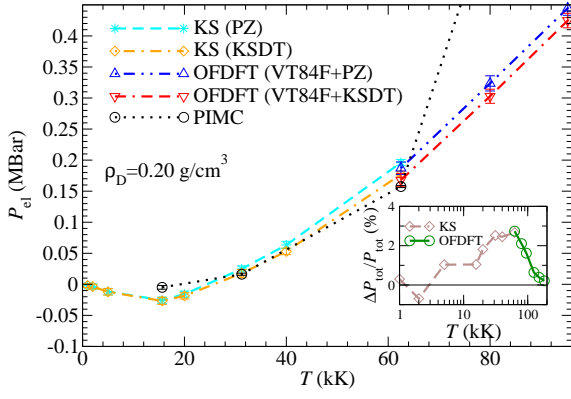


FIG. 6: Deuterium electronic pressure as a function of  $T$  from KS and OFDFT calculations with the finite- $T$  KSDT and ground-state PZ XC functionals. Inset: relative difference between total pressure from the calculations with the PZ and KSDT XC; see Eq. (8). System density  $\rho_D = 0.20 \text{ g/cm}^3$  ( $r_s = 3$  bohr). PIMC results are shown for comparison.

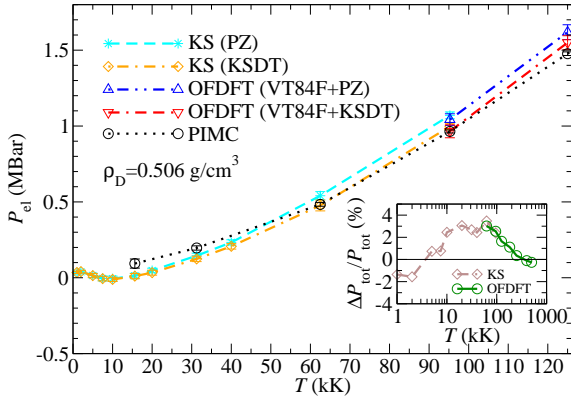


FIG. 7: As in Fig. (6) for Deuterium,  $\rho_D = 0.506 \text{ g/cm}^3$  ( $r_s = 2.2$  bohr).

several temperatures, we also did 8500 step simulations to test pressure convergence. The time step was scaled with increasing  $T$  by a factor proportional to  $1/\sqrt{T}$ .

Figures 6 - 10 compare the *electronic* pressure (that is, without the ionic ideal gas contribution) from the KS and OFDFT calculations done in conjunction with the finite- $T$  KSDT and ground-state PZ XC functionals. Error bars shown in those figures correspond to the standard deviation for the average *electronic* pressure. The insets show the percentage relative difference for the calculated *total* pressures (i.e., including the thermal ionic contribution), namely

$$\Delta P_{\text{tot}}/P_{\text{tot}} \equiv (P_{\text{tot}}^{\text{PZ}} - P_{\text{tot}}^{\text{KSDT}})/P_{\text{tot}}^{\text{PZ}} \times 100\%. \quad (8)$$

That quantity measures the XC thermal effects upon the *total* pressure in the system.

Note first that the relative difference  $\Delta P_{\text{tot}}$  is of both signs, so no simple offset can be used as a correction. Sjoström and Daligault [21] found pressure differences of both signs as well, whereas Ref. [22] did not. We at-

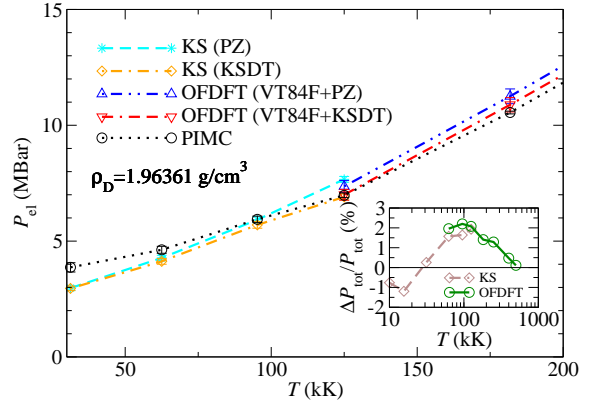


FIG. 8: As in Fig. (6) for Deuterium,  $\rho_D = 1.964 \text{ g/cm}^3$  ( $r_s = 1.4$  bohr).

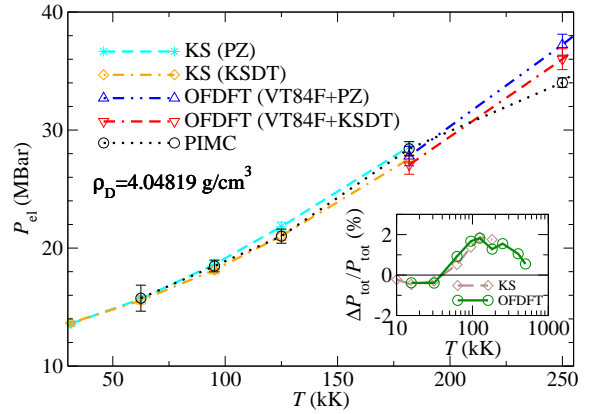


FIG. 9: As in Fig. (6) for Deuterium,  $\rho_D = 4.04819 \text{ g/cm}^3$  ( $r_s = 1.10$  bohr).

tribute the difference to the limitations of the  $\mathcal{F}_{\text{xc}}$  functional used in the latter work.  $\Delta P_{\text{tot}}$  is largest at the lowest densities, with a range of about 6% for both  $0.20$  and  $0.506 \text{ g/cm}^3$ . That range decreases to about 3% (still with both signs) at  $\rho_D = 1.9631 \text{ g/cm}^3$ , then it continues down to about 2% at  $\rho_D = 4.04819 \text{ g/cm}^3$  and is 1% at most for  $\rho_D = 10.0 \text{ g/cm}^3$ . (For reference, the equilibrium simple cubic density at  $T \approx 0\text{K}$  is about  $1 \text{ g/cm}^3$ .) Of course, the relative pressure shift is practically negligible at low  $T$  because the low- $T$  limit of KSDT was designed to recover the ground-state LDA. (Ref. [14] gives a comparison of the KSDT and PZ correlation energies at  $T = 0 \text{ K}$ .)

The overall behavior is clear.  $T$ -dependent XC first raises the pressure, then, as  $T$  increases, it lowers the pressure compared to that generated by a ground state XC before both go to a common high- $T$  limit. That limit occurs at much higher  $T$  than what is shown in Figs. 6-10. That limiting behavior occurs even though the two approximate functionals, KSDT and PZ, have different high- $T$  limits. But the XC contribution becomes negligible compared to the non-interacting free-energy contribution at high- $T$ , so the effect of those different limits is

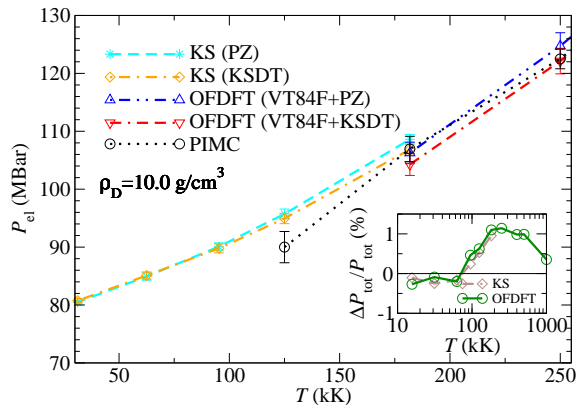


FIG. 10: As in Fig. (6) for Deuterium,  $\rho_D = 10.0 \text{ g/cm}^3$  ( $r_s = 0.81373 \text{ bohr}$ ).

suppressed. There is some intermediate  $T$  at which there is no shift between the two functionals (see discussion of Fig. 15 below; also see Ref. 39). The well-defined maxima of the total pressure relative differences occur near  $T \approx 40 \text{ kK}$ ,  $60 \text{ kK}$ ,  $100 \text{ kK}$ ,  $125 \text{ kK}$ , and  $200 \text{ kK}$  for  $r_s = 3, 2.20, 1.40, 1.10$ , and  $0.81373 \text{ bohr}$  respectively, with corresponding values of about 3, 4, 2.5, 2 and 1 %. Note also the nice correlation of the XC thermal effect upon the pressure with Fig. 1. The maximum effect occurs approximately along the lower edge of the yellow-orange band and the maximum magnitude decreases with decreasing  $r_s$ .

We note also that the OFDFT finite  $T$  results at high  $T$  are in good overall agreement with PIMC simulation data [5]. The PIMC calculations should describe the  $T$ -dependence of all free-energy terms correctly, including the electron-electron interaction and therefore, the XC free energy. Figs. 6 - 10 demonstrate that inclusion of the  $T$ -dependent XC provides overall better agreement between the KS and PIMC data than does use of ground-state XC. The exception is points where PIMC clearly exhibits irregular behavior. That occurs at low- $T$  for some material densities, with the PIMC pressures seeming to be significant overestimates relative to the KS results for  $r_s = 3 \text{ bohr}$  (see Fig. 6),  $r_s = 2.20 \text{ bohr}$  (see Fig. 7), and  $r_s = 1.40 \text{ bohr}$  (see Fig. 8). For  $r_s = 0.81373 \text{ bohr}$  the PIMC pressure is low relative to KS at the lowest available temperature  $T = 125 \text{ kK}$ .

### C. Hugoniot of liquid Hydrogen

Experimentally the EOS at high compressions is accessible via shock-wave techniques and the Hugoniot relation

$$\mathcal{E} - \mathcal{E}_0 - \frac{1}{2}(P + P_0) \left( \frac{1}{\rho} - \frac{1}{\rho_0} \right) = 0, \quad (9)$$

where  $\mathcal{E}$ ,  $P$ , and  $\rho$  are the specific *internal* energy, pressure, and bulk density of a state derived by shock compression from an initial state at  $\rho_0$ ,  $\mathcal{E}_0$ , and  $P_0$ .

TABLE I: Pressure (kBar), atomization energy  $D_e$  (eV/molecule), and corresponding ZPE-corrected  $\mathcal{E}_0$  (in kJ/g) obtained from MD simulations for Hydrogen at  $\rho_0 = 0.0855 \text{ g/cm}^3$ ,  $T = 20 \text{ K}$  with different codes/functionals. “QE” is Quantum Espresso. All cases used PAWs.

Code	XC	$P_0$	$D_e^a$	$\mathcal{E}_0$
QE	PZ	-2.2	-6.7370	-310.0 <sup>b</sup>
QE	KSDT	-2.3	-6.7264	-309.5 <sup>b</sup>
QE	PBE	0.25	-6.7703	-311.3 <sup>c</sup>
VASP	PBE	0.21	-6.7756	-311.5 <sup>c</sup>
VASP	PBE			-314 <sup>d</sup>

$$^a D_e = (E_{np}(H_{64}) - 64E_{np}(H))/32.$$

$$^b \text{ZPE correction } E_{vib} = \omega_e^{\text{LDA}}/2 = 0.260 \text{ eV}.$$

$$^c \text{ZPE correction } E_{vib} = \omega_e^{\text{PBE}}/2 = 0.267 \text{ eV}.$$

<sup>d</sup>Ref. 12.

The initial state presents some technical challenges for computation. To enable a meaningful comparison between energies of states calculated from different codes (and possibly with different pseudopotentials),  $\mathcal{E}_0$  and  $\mathcal{E}$  usually are calculated as effective atomization energies of the system. Doing so provides some error cancellation, especially for approximate treatment of core electronic states. Additionally, zero-point vibrational energy (ZPE) corrections are needed. For Hydrogen, the result is that the initial state specific energy takes the form

$$\mathcal{E}_0 = \frac{E(H_N) + NE_{vib}/2 - NE(H)}{Nm_H}, \quad (10)$$

where  $E_{vib}$  is the ZPE for the  $H_2$  diatomic molecule,  $E(H_N)$  is the energy of the  $N$ -atom system corresponding to the initial conditions at material density  $\rho_0$  and temperature  $T_0$ ,  $E(H)$  is the energy of an isolated H atom of mass  $m_H$ . Note that  $E(H)$  can be from a spin-polarized or non-spin-polarized calculation, because eventually these terms cancel in Eq. (9). Table I shows atomization energies ( $D_e = 2\{E_{np}(H_N) - NE_{np}(H)\}/N$ ) from the non-spin-polarized calculation ( $E_{np}$ ), and values of pressure and energy  $\mathcal{E}_0$  corresponding to the initial state with  $\rho_0 = 0.0855 \text{ g/cm}^3$  at  $T_0 = 20 \text{ K}$  (essentially equilibrium bulk  $H_2$ ). In terms of  $D_e$ , the specific energy of the initial state is given by  $\mathcal{E}_0 = (D_e + E_{vib})/2m_H$ . The vibrational correction is from the theoretical ZPE obtained from DFT vibrational frequency calculations for the  $H_2$  molecule with the aug-cc-pVQZ basis set [53], using the Vosko-Wilk-Nusair LDA [54] and Perdew-Burke-Ernzerhof (PBE)[55] GGA functionals. We remark that  $\mathcal{E}_0$  values in Table I are shifted by  $E_{np}(H)/m_H$  with respect both to  $E(H_{64})/64m_H$  (see Eq. (10)) and to the value reported in Ref. [56] and used in Ref. [22]. For example, for 32  $H_2$  molecules at initial conditions used here, our QuantumEspresso calculation with PZ XC gives -31.009 eV/molecule or -15.505 eV/atom. Correcting by the 0.260 eV/molecule ZPE gives -15.375 eV/atom, equivalent to  $\mathcal{E}_0 = -1472 \text{ kJ/g}$  unshifted value.

Figure 11 compares the Hydrogen principal Hugoniot from the simulations with the KSDT and PZ XC func-



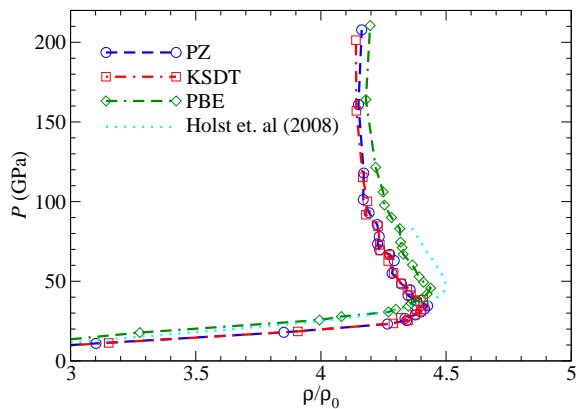


FIG. 11: Hydrogen principal Hugoniot. Initial density  $\rho_0 = 0.0855 \text{ g/cm}^3$ .

tionals. Results for the PBE GGA XC (also with  $T$ -dependent density) are shown to provide an alternative perspective on the effects of changing only the XC approximation. For  $T < 30 \text{ kK}$ , there is little XC thermal effect. For example, the maximum compression is 4.41 for KSDT versus 4.43 for PZ at  $P \approx 35 \text{ GPa}$ . Shifting from LDA to GGA (both ground-state functionals, PZ vs. PBE) changes the result only to 4.44 (PBE) but at notably higher pressure,  $P \approx 46 \text{ GPa}$ . For  $T \geq 30 \text{ kK}$  ( $P \geq 120 \text{ GPa}$ ),  $P$  and  $T$  increase practically at constant compression for all three curves. The  $T$ -dependent XC predicts slightly lower pressures than those from PZ, in agreement with the results shown in Sec. III B. This can be seen in the upper panel of Fig. 12, which displays  $P(T)$  along the Hugoniot. At  $T = 30 \text{ kK}$  the effects on  $P$  of  $T$ -dependence in XC versus shifting to gradient corrections in XC are comparable. As  $T$  increases, gradient corrections diminish in importance and the PZ and PBE curves become closer. In contrast, the effect of explicit  $T$ -dependence continues to increase. The lower panel of Fig. 12 shows the same comparison for the specific *internal* energy (relative to the reference state). At low  $T$ , the KSDT internal energy is slightly higher than the PZ result whereas at high  $T$  the reverse is true. Overall the two yield nearly identical values. That helps explain why the Hugoniot curve, Fig. 11, is insensitive to the use of KSDT rather than PZ XC. In the region of primary interest, KSDT lowers both quantities on the LHS of Eq. 9,  $P$  and  $\mathcal{E}$ , relative to PZ XC values, such that the solution, the material density  $\rho$ , remains almost unchanged as compared to PZ XC results. This insensitivity of the Hugoniot to  $T$ -dependence in XC agrees with the findings of Ref. 57, namely that the Hugoniot is determined mainly by the statistics of nuclear configurations, not by the electronic  $T$ .

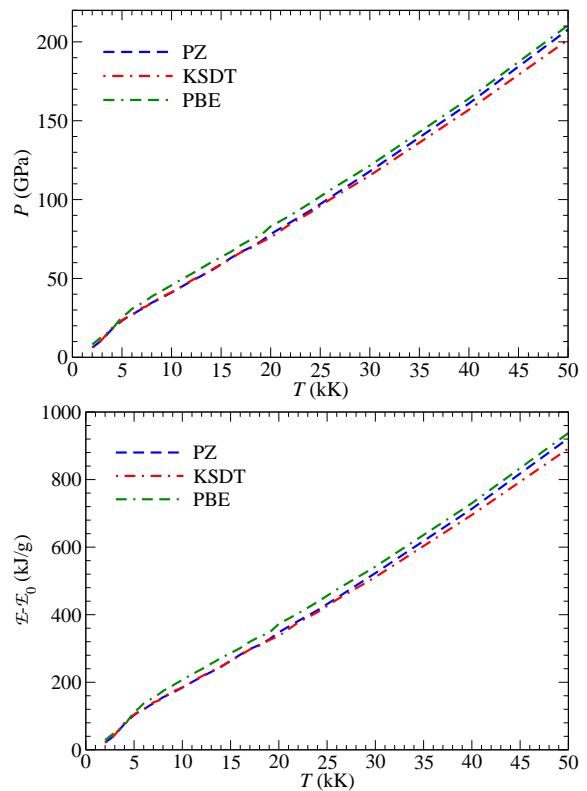


FIG. 12: Pressure (upper panel) and specific *internal* energy difference (lower panel) along the Hydrogen Hugoniot as functions of  $T$ .

#### D. Homogeneous and in-homogeneous electron gas at finite $T$

Insight into the behaviors discussed in the preceding sections may be gained by going back to basics, namely the HEG. The KSDT functional Eq. (1) is itself an accurate parametrization of RPIMC simulation data for the finite- $T$  HEG. Closely related to the HEG is static bulk atomic H, a hypothetical system we have used to test OFDFT non-interacting free-energy functionals. The system is an abstraction of the experimental coexistence of hot electrons and cold ions that can occur with femtosecond laser pulses [3].

For the HEG, consider first its bulk equilibrium density as a function of  $T$ , i.e., that value of  $r_s$  for which the HEG free energy per particle is minimum. Figure 13 shows this free energy per particle ( $f = f_s + f_{xc}$ ) as a function of  $r_s$  for selected temperatures calculated with the KSDT functional. The upper panel of Fig. 14 shows the difference for equilibrium  $r_s$  between KSDT and PZ. At  $T = 0 \text{ K}$  the equilibrium  $r_{s, \text{equilib}} = 4.19 \text{ bohr}$  for both XC functionals (see also Ref. 41). The value remains almost constant up to  $T \approx 1000 \text{ K}$ . The ground-state PZ result starts to deviate from the finite- $T$  KSDT values at  $T \approx 4000 \text{ K}$ . The HEG explodes, in the sense that the  $r_{s, \text{equilib}}$  increases drastically at about

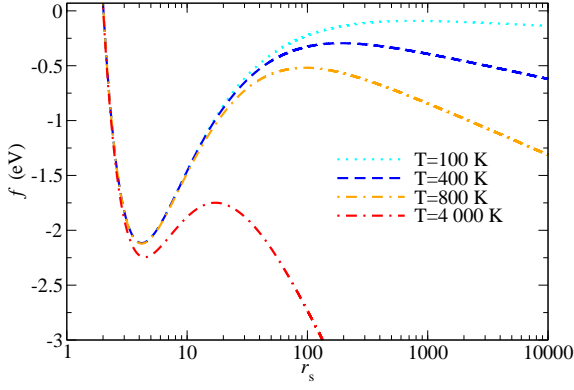


FIG. 13: HEG total free-energy per electron as a function of  $r_s$  for selected temperatures calculated with the KSDT XC functional.

$T_c \approx 7200\text{K}$  for the finite- $T$  XC. Use of the ground-state PZ XC approximation lowers that substantially, to about  $6200\text{K}$ . What may be construed as the HEG binding energy is shown in the lower panel of Fig. 14. The quantity  $\Delta f$  shown there is the depth of the minimum of the total free-energy per particle (see Fig. 13) relative to the maximum at lower density (higher  $r_s$ ). As Fig. 13 shows, one may also construe  $\Delta f$  as a barrier height. For both KSDT and PZ XC,  $\Delta f$  decreases with increasing  $T$  starting from 1 eV at  $T=0$  K and plunging to essentially zero at the same critical values of  $T$  as before, about  $7200$  K for KSDT vs.  $6200$  K for PZ, a 14% shift. Given the structureless nature of the HEG, these comparisons drive home the point that the low density regime is rather sensitive to XC thermal effects.

Effects of reduction in translational invariance to periodic are illuminated by considering simple cubic bulk atomic Hydrogen (“sc-H” hereafter). In essence, it is an inhomogeneous electron gas with the simplest conceivable point charge compensating background. Figure 15 shows the equilibrium  $r_s$  as a function of  $T$ . The behavior is similar to that for the HEG, namely a monotonic increase of the equilibrium  $r_s$  with increasing  $T$  and substantially lower values of the equilibrium  $r_s$  from the  $T$ -dependent KSDT XC than from PZ XC at high- $T$  ( $20 \text{ kK} < T < 30 \text{ kK}$ ). For  $5 \text{ kK} < T < 15 \text{ kK}$  the situation reverses, with KSDT giving slightly larger  $r_s$  values than PZ. Thus either the pressures or the equilibrium  $r_s$  values from the two XC approximations will coincide at some intermediate  $T$ . Such behavior was observed previously for bcc-Li (see Fig. 11 in Ref. 39) and is consistent with the AIMD results discussed above (recall Section III B). For  $T > 30\text{kK}$  the sc-H model becomes unstable. Replacement of the uniform background in the case of HEG with compensating point charges in sc-H makes the average equilibrium density at  $T = 0$  K of the sc-H much higher than for the HEG ( $r_{s,\text{equilib}} = 4.19$  bohr for the HEG vs.  $1.70$  bohr for sc-H), hence sc-H is stable to much higher  $T$  ( $T_{c,\text{sc-H}} \approx 30\,000$  K vs.  $T_{c,\text{HEG}} \approx 7200$

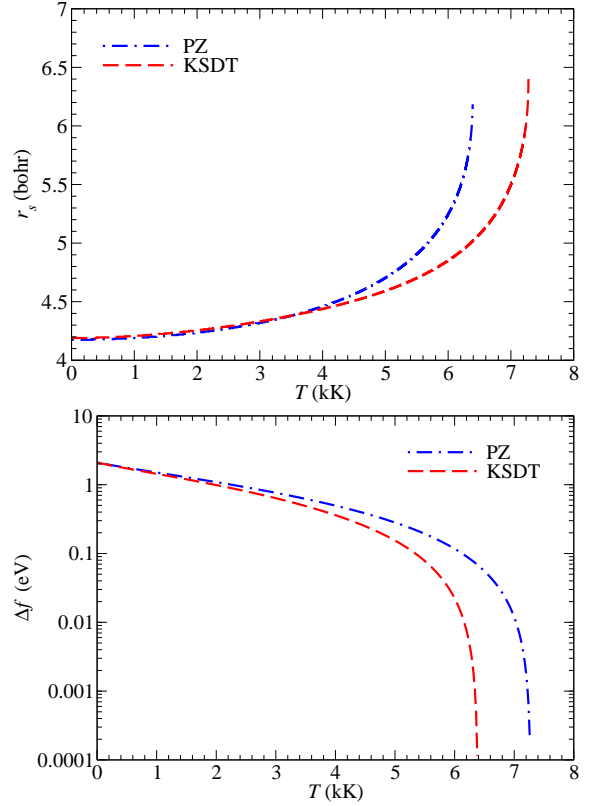


FIG. 14: Upper panel: value of equilibrium  $r_s$  corresponding to the minimum of the total free-energy per electron for the HEG as a function of  $T$ . Lower panel: HEG barrier height (binding energy; see Fig. 13 and see text) as function of  $T$ .

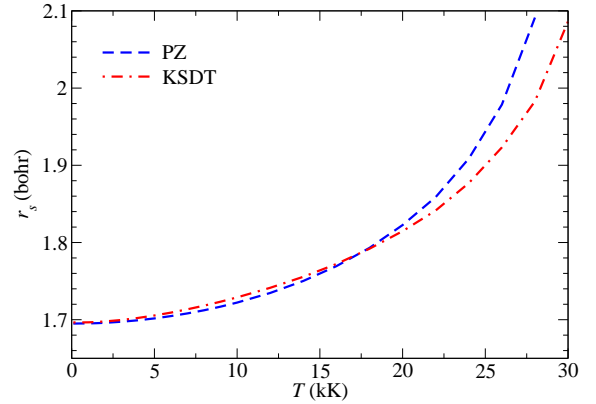


FIG. 15: Equilibrium  $r_s$  as a function  $T$  for sc-H. See text.

K). Compare Figs. 14 and 15.

Finally, we consider the sc-H electronic heat capacity at constant volume as a function of electronic temperature  $T$ .

$$C_V^{el} = (\partial \mathcal{E}^{el} / \partial T)_V. \quad (11)$$

It obviously is a measure of the  $T$ -dependence of the electronic internal energy  $\mathcal{E}^{el}$ , which of course has an XC contribution  $\mathcal{E}_{xc}$ . That  $T$ -dependence is qualitatively

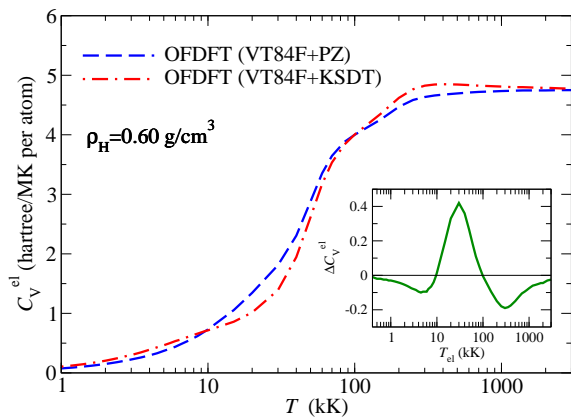


FIG. 16: Electronic heat capacity at constant volume  $C_V^{el}$  as a function of electronic temperature for sc-H at material density  $\rho_H = 0.60 \text{ g/cm}^3$  with the finite- $T$  KSDT and ground-state PZ XC functionals. The inset shows the difference  $\Delta C_V^{el} = C_V^{el,PZ} - C_V^{el,KSDT}$ .

different for the zero- $T$  and finite- $T$  XC functionals (see Refs. 14, 39).  $C_V^{el}$  therefore provides a different direct measure of XC thermal effects from that provided by quantities considered thus far. Figure 16 compares  $C_V^{el}$  obtained from the KSDT and PZ XC functionals for sc-H. These were done with OFDFT using the VT84F non-interacting free-energy functional [36]. The maximum magnitude of the difference  $\Delta C_V^{el} = C_V^{el,PZ} - C_V^{el,KSDT}$  for  $\rho_H = 0.60 \text{ g/cm}^3$  is 0.4 hartree/MK at  $T \approx 30 \text{ kK}$ . That corresponds to about a 40% relative difference. In the zero- $T$  and high- $T$  limits the difference between the KSDT and PZ XC results vanishes as expected. Notice how those limits lead to broad consistency of behavior with respect to other quantities discussed above. XC thermal effects relative to a ground-state functional are quite variable in magnitude. For  $C_V^{el}$  the difference is manifested both as a maximum and as two other extrema of lesser magnitude.

#### IV. CONCLUDING REMARKS

The increase in resistivity of Al at  $0.1 \text{ g/cm}^3$  found in Ref. 18 upon going from the VWN ground-state XC functional [54] to the Perrot-Dharma-wardana (PDW)  $T$ -dependent functional [25] is qualitatively consistent with our finding of the lowered DC conductivity of low-density Al. Quantitatively, however, the results are quite different. In particular, the low- $T$  behavior of the resistivity calculated from the PDW functional is drastically different from our KSDT result, their VWN result, and Perrot and Dharma-wardana's earlier calculation [58]. We suspect methodological differences but can not say more.

Ref. 59 included an analysis suggesting that intrinsic  $T$ -dependence in  $\mathcal{F}_{xc}$  did not necessarily mean there

would be a corresponding impact on the  $T$ -dependence of the Kubo-Greenwood optical conductivity. The nub of that argument was that the conductivity depends on the KS eigenvalues and orbitals, which are determined by the KS potential (for which the XC contribution is  $v_{xc} = \delta\mathcal{F}_{xc}/\delta n$ ). Sums of matrix elements over such KS quantities do not necessarily have a strong sensitivity to  $T$ -dependence of  $\mathcal{F}_{xc}$ .

Such arguments tend to overlook state conditions. Here, we have given an example of a system for which  $\sigma_{DC}$  has a stronger sensitivity (in the sense of percentage shift) to XC thermal effects in a pertinent range of thermodynamic conditions than does the EOS of a different system over a different but also pertinent range of thermodynamic conditions. This shows that both system definition and state conditions are essential for proper assessment of the GSA.

For the DC conductivity of low-density Al, XC thermal effects incorporated in the KSDT functional increase inter-band separations relative to GSA above the Fermi level, hence decrease the Fermi-Dirac occupations relative to GSA. That lowers the calculated conductivity (see Eq. (6)), and thereby yields better agreement with the experimental data. We remark that the ground-state functionals underestimate band gaps, while hybrid functionals (which incorporate a fraction of exact single-determinant exchange, thus take into account a part of exchange thermal effects) enlarge such intervals. Therefore one expects that a hybrid functional would lower the conductivity. Notice that in the case of thermal Hartree-Fock, thermal occupation at temperatures of 1 or 2 eV *reduces* the spuriously large inter-band separations of ground-state HF states [39]. That, in turn, would drive the opposite trend, *increasing* the conductivity. Interestingly, the overall XC thermal effect upon the DC conductivity of low density Al is to reduce the range of the  $T$ -variation at fixed bulk density. In contrast, at higher material density the Al DC conductivity is essentially insensitive to the XC  $T$ -dependence.

The Deuterium EOS calculations show that XC thermal effects must be taken into account in thermodynamic conditions corresponding approximately to the reduced temperature  $t \approx 0.5$ . However, because the principal Hugoniot characterizes the difference of two states separated by a shock, there is a cancellation that is familiar in other uses of KS-DFT (e.g., atomization energies) which substantially suppresses the XC thermal effects. As noted above, this cancellation is consistent with the findings of Tubman *et al.* [57] and with Danel *et al.* [22]. We suspect therefore that the XC thermal effects on the Al Hugoniot found in Ref. 17 and on the Be Hugoniot in Ref. 19 are consequences of the techniques they used. In the former work  $T$ -dependence was introduced by adding jellium shifts to the energy and pressure at  $r_s$  corresponding to the density at hand. The second used an average atom. Nevertheless the XC thermal effects on the pressure  $P(T)$  (recall upper panel of Fig. 12) are not negligible. Rather the pressure effect is about the

same magnitude as the shift from gradient-independent to gradient-dependent XC. This also is consistent with what is reported by Danel *et al.* [22]. More accurate predictions (for all properties affected by the XC thermal effects) will require both explicit  $T$ -dependence and gradient contributions in the XC functional, at least.

Even at the LDA level of refinement, however, it is clear that the GSA (use of a ground-state XC functional as an approximate free-energy XC functional) is not an unequivocally valid prescription [13]. That assessment is consistent with earlier demonstrations of the non-trivial  $T$ -dependence of the XC free-energy [14, 39, 60]. It also confirms what one knows in principle, namely that consistent study of WDM requires an approximate  $\mathcal{F}_{xc}$  which has a proper high- $T$  limit, a correct small- $r_s$  limit, a correct small- $\Gamma$  (the dimensionless Coulomb coupling parameter) limit, and delivers a properly positive entropy. The KSDT functional is built with the first three included explicitly and is found to satisfy the last *a posteriori* in every case considered.

## V. ACKNOWLEDGMENTS

We thank Debajit Chakraborty and Travis Sjoström for helpful comments on the manuscript and Jim Dufty

and Mike Desjarlais for helpful discussions regarding optical conductivity calculations. We thank Kieron Burke for providing the revised version of Ref. 13 and for alerting us to the entropy negativity discussed in Sect. II C. We thank an anonymous referee for noting the expected effect of hybrid XC functionals upon interband separations and, thereby, the DC conductivity. Our work was supported by U.S. Dept. of Energy grant de-sc0002139. We thank the University of Florida Research Computing organization for computational resources and technical support. The most demanding optical conductivity calculations were feasible only because of resources provided by the National Energy Research Scientific Computing Center, a DOE Office of Science User Facility supported by the Office of Science of the U.S. Department of Energy under Contract No. de-sc0002139.

- 
- [1] R.L. McCrory, D.D. Meyerhofer, R. Betti, R.S. Craxton, J.A. Delettrez, D.H. Edgell, V.Yu. Glebov, V.N. Goncharov, D.R. Harding, D.W. Jacobs-Perkins, J.P. Knauer, F.J. Marshall, P.W. McKenty, P.B. Radha, S.P. Regan, T.C. Sangster, W. Seka, R.W. Short, S. Skupsky, V.A. Smalyuk, J.M. Soures, C. Stoeckl, B. Yaakobi, D. Shvarts, J.A. Frenje, C.K. Li, R.D. Petrasso, and F.H. Séguin, *Phys. Plasmas* **15**, 055503 (2008).
- [2] J. Lindl, *Phys. Plasmas* **2**, 3933 (1995).
- [3] R. Ernstorfer, M. Harb, C.T. Hebeisen, G. Sciaini, T. Dartigalongue, and R.J.D. Miller, *Science* **323**, 1033 (2009).
- [4] R. Kodama, P.A. Norreys, K. Mima, A.E. Dangor, R.G. Evans, H. Fujita, Y. Kitagawa, K. Krushelnick, T. Miyakoshi, N. Miyanaga, T. Norimatsu, S.J. Rose, T. Shozaki, K. Shigemori, A. Sunahara, M. Tambo, K.A. Tanaka, Y. Toyama, T. Yamanaka, and M. Zepf, *Nature* **412**, 798 (2001).
- [5] S.X. Hu, B. Militzer, V.N. Goncharov, and S. Skupsky, *Phys. Rev. B* **84** 224109 (2011).
- [6] S. Chang, *Physics Today* **68**, 12 (2015).
- [7] N.D. Mermin, *Phys. Rev.* **137**, A1441 (1965).
- [8] M.V. Stoitsov and I.Zh. Petkov, *Annals Phys.* **185**, 121 (1988).
- [9] R.M. Dreizler in *The Nuclear Equation of State, Part A*, W. Greiner and H. Stöcker eds., NATO ASI **B216** (Plenum, NY, 1989) 521.
- [10] M.P. Desjarlais, J.D. Kress, and L.A. Collins, *Phys. Rev. E* **66**, 025401 (2002).
- [11] S. Mazevet, M.P. Desjarlais, L.A. Collins, J.D. Kress, and N.H. Magee, *Phys. Rev. E* **71**, 016409 (2005).
- [12] B. Holst, R. Redmer, and M.P. Desjarlais, *Phys. Rev. B* **77**, 184201 (2008).
- [13] K. Burke, J.C. Smith, P.E. Grabowski, and A. Pribram-Jones, arXiv:1511.02194; revised version private communication K. Burke to S. Trickey, 03 Feb. 2016.
- [14] V.V. Karasiev, T. Sjoström, J. Dufty, and S.B. Trickey, *Phys. Rev. Lett.* **112**, 076403 (2014).
- [15] J.P. Perdew, and A. Zunger, *Phys. Rev. B* **23**, 5048 (1981).
- [16] R.P. Feynman, N. Metropolis, and E. Teller, *Phys. Rev.* **75**, 1561 (1949).
- [17] M.P. Surh, T.W. Barbee III, and L.H. Yang, *Phys. Rev. Lett.* **86**, 5958 (2001).
- [18] P. Renaudin, C. Blancard, G. Faussurier, and P. Noiret, *Phys. Rev. Lett.* **88**, 215001 (2002).
- [19] P.A. Sterne, S.B. Hansen, B.G. Wilson, and W.A. Isaacs, *High Energy Density Phys.* **3**, 278 (2007).
- [20] G. Faussurier, P.L. Silvestrelli, and C. Blancard, *High Energy Density Phys.* **5**, 74 (2009).
- [21] T. Sjoström, and J. Daligault, *Phys. Rev. B* **90**, 155109 (2014).
- [22] J.-F. Danel, L. Kazandjian, and R. Piron, *Phys. Rev. E* **93**, 043210 (2016).
- [23] S. Tanaka, S. Mitake, and S. Ichimaru, *Phys. Rev. A* **32**, 1896 (1985).
- [24] S. Ichimaru, H. Iyetomi, and S. Tanaka, *Phys. Repts.* **149**, 91 (1987).
- [25] F. Perrot and M.W.C. Dharma-wardana, *Phys. Rev. A* **30**, 2619 (1984).
- [26] F. Perrot and M.W.C. Dharma-wardana, *Phys. Rev. B* **62**, 16536 (2000); F. Perrot and M.W.C. Dharma-



- wardana, Phys. Rev. B **67**, 079901(E) (2003).
- [27] E.W. Brown, B.K. Clark, J.L. DuBois, and D.M. Ceperley, Phys. Rev. Lett. **110**, 146405 (2013).
- [28] G.G. Spink, R.J. Needs, and N.D. Drummond, Phys. Rev. B **88**, 085121 (2013).
- [29] T. Schoof, S. Groth, J. Vorberger, and M. Bonitz, Phys. Rev. Lett. **115**, 130402 [6 pp] (2015).
- [30] V.V. Karasiev, T. Sjostrom, and S.B. Trickey, Comput. Phys. Commun. **185**, 3240 (2014).
- [31] Paolo Giannozzi, Stefano Baroni, Nicola Bonini, Matteo Calandra, Roberto Car, Carlo Cavazzoni, Davide Ceresoli, Guido L. Chiarotti, Matteo Cococcioni, Ismaila Dabo, Andrea Dal Corso, Stefano de Gironcoli, Stefano Fabris, Guido Fratesi, Ralph Gebauer, Uwe Gerstmann, Christos Gougousis, Anton Kokalj, Michele Lazzeri, Layla Martin-Samos, Nicola Marzari, Francesco Mauri, Riccardo Mazzarello, Stefano Paolini, Alfredo Pasquarello, Lorenzo Paulatto, Carlo Sbraccia, Sandro Scandolo, Gabriele Scaluzero, Ari P. Seitsonen, Alexander Smogunov, Paolo Umari, and Renata M. Wentzcovitch, J. Phys.: Condens. Matter **21**, 395502 (2009).
- [32] G.S. Ho, V.L. Lignères, and E.A. Carter, Comput. Phys. Commun. **179**, 839 (2008).
- [33] L. Hung, C. Huang, I. Shin, G.S. Ho, V.L. Lignères, and E.A. Carter, Comput. Phys. Commun. **181**, 2208 (2010).
- [34] <http://www.qtp.ufl.edu/ofdf/research/computation.shtml>
- [35] M.A.L. Marques, M.J.T. Oliveira, and T. Burnus, Comp. Phys. Commun. **183**, 2272 (2012).
- [36] V.V. Karasiev, D. Chakraborty, O.A. Shukruto, and S.B. Trickey, Phys. Rev. B **88**, 161108(R) (2013).
- [37] V.V. Karasiev (unpublished).
- [38] F. Jollet, M. Torrent, N. Holzwarth, Comput. Phys. Commun. **185**, 1246 (2014).
- [39] V.V. Karasiev, T. Sjostrom, and S.B. Trickey, Phys. Rev. E **86**, 056704 (2012).
- [40] V.V. Karasiev, T. Sjostrom, and S.B. Trickey, Phys. Rev. B **86**, 115101 (2012).
- [41] J.P. Perdew, and Y. Wang, Phys. Rev. B **45**, 13244 (1992).
- [42] L. Goodwin, R.J. Needs, and V. Heine, J. Phys.: Condens. Matter **2**, 351 (1990).
- [43] V.V. Karasiev and S.B. Trickey, Comput. Phys. Commun. **183**, 2519 (2012).
- [44] R. Kubo, J. Phys. Soc. Jpn. **12**, 570 (1957).
- [45] D.A. Greenwood, Proc. Phys. Soc. **71**, 585 (1958).
- [46] X. Gonze, B. Amadon, P.-M. Anglade, J.-M. Beuken, F. Bottin, P. Boulanger, F. Bruneval, D. Caliste, R. Caracas, M. Cote, T. Deutsch, L. Genovese, Ph. Ghosez, M. Giantomassi, S. Goedecker, D.R. Hamann, P. Hermet, F. Jollet, G. Jomard, S. Leroux, M. Mancini, S. Mazevet, M.J.T. Oliveira, G. Onida, Y. Pouillon, T. Rangel, G.-M. Rignanese, D. Sangalli, R. Shaltaf, M. Torrent, M.J. Verstraete, G. Zerah, and J.W. Zwanziger, Comput. Phys. Commun. **180**, 2582 (2009); X. Gonze, G.-M. Rignanese, M. Verstraete, J.-M. Beuken, Y. Pouillon, R. Caracas, F. Jollet, M. Torrent, G. Zerah, M. Mikami, Ph. Ghosez, M. Veithen, J.-Y. Raty, V. Olevano, F. Bruneval, L. Reining, R. Godby, G. Onida, D.R. Hamann, and D.C. Allan, Zeit. Kristallogr. **220**, 558 (2005).
- [47] M. Torrent, F. Jollet, F. Bottin, G. Zerah, and X. Gonze, Comput. Mat. Sci. **42**, 337 (2008).
- [48] S. Mazevet, M. Torrent, V. Recoules, and F. Jollet, High Energy Density Phys. **6**, 84 (2010).
- [49] H.J. Monkhorst and J.D. Pack, Phys. Rev. B **13**, 5188 (1976).
- [50] A. Baldereschi, Phys. Rev. B **7**, 5212 (1973).
- [51] A.W. DeSilva, and J.D. Katsourous, Phys. Rev. E **57**, 5945 (1998).
- [52] F. Lambert, V. Recoules, A. Decoster, J. Cléroutin, and M. Desjarlais, Phys. Plasmas **18**, 056306 (2011).
- [53] T.H. Dunning, Jr., J. Chem. Phys. **90**, 1007 (1989); R.A. Kendall, T.H. Dunning, Jr., and R.J. Harrison, *ibid.* **96**, 6796 (1992).
- [54] S.H. Vosko, L. Wilk, and M. Nusair, Can. J. Phys. **58**, 1200 (1980).
- [55] J.P. Perdew, K. Burke, and M. Ernzerhof, Phys. Rev. Lett. **77**, 3865 (1996); erratum *ibid.* **78**, 1396 (1997).
- [56] W. Kołos, and L. Wolniewicz, J. Chem. Phys. **41**, 3674 (1964).
- [57] N.M. Tubman, E. Liberatore, C. Pierleoni, M. Holzmann, and D.M. Ceperley, Phys. Rev. Lett. **115**, 045301 (2015).
- [58] F. Perrot and M.W.C. Dharma-wardana, Phys. Rev. A **36**, 238 (1987).
- [59] V.V. Karasiev, T. Sjostrom, D. Chakraborty, J.W. Dufty, K. Runge, F.E. Harris, and S.B. Trickey, in *Frontiers and Challenges in Warm Dense Matter*, Series: *Lecture Notes in Computational Science and Engineering*, **96**, edited by F. Graziani, M.P. Desjarlais, R. Redmer, and S.B. Trickey (Springer 2014), p. 61.
- [60] T. Sjostrom, F.E. Harris, and S.B. Trickey, Phys. Rev. B **85**, 045125 (2012).